Measurement of surface deformation related to the December 2018 Mt. Etna eruption using time-series interferometry and magma modeling for hazard zone mapping

Suci Ramayanti[1], Arief R. Achmad[2], Hahn Chul Jung[3], Min-Jeong Jo[4], Sang-Wan Kim[5], Yu-Chul Park[6], and Chang-Wook Lee[1,2]*

[1]Department of Science Education, Kangwon National University, Chuncheon-si, Gangwon-do 24341, Republic of Korea
[2]Department of Smart Regional Innovation, Kangwon National University, Chuncheon-si, Gangwon-do 24341, Republic of Korea
[3]Korea Ocean Satellite Center, Korea Institute of Ocean Science and Technology, Busan 49111, Republic of Korea
[4]Biospheric Sciences Laboratory, NASA Goddard Space Flight Center, Greenbelt, MD 20771, USA
[5]Department of Energy Resources and Geosystems Engineering, Sejong University, Seoul 05006, Republic of Korea
[6]Department of Geophysics, Kangwon National University, Chuncheon-si, Gangwon-do 24341, Republic of Korea

ABSTRACT: Mount Etna has erupted several times since it was first formed. Recently, Mount Etna began erupting again over 24–27 December 2018. Because it erupts frequently, Mount Etna should be observed on a frequent basis. From June 2018 to October 2019, 34 and 56 interferometric synthetic aperture radar (InSAR) images were acquired from the ascending and descending tracks of the Sentinel-1 satellite, respectively. We employed the Stanford Method for Persistent Scatterers (StaMPS) and a refined small baseline subset (SBAS) InSAR method to produce a surface deformation time-series map. In the time-series analysis, the phase signal remained unaltered with time. The Okada model was then applied to the result to generate a modeled interferogram, and the Q-LavHA program was run to generate a lava flow prediction model. A direct comparison of the results showed that Persistent Scatterers Interferometry (PSI)-StaMPS and the refined SBAS technique were comparable in terms of the displacement pattern, with slightly different velocity values obtained for individual points. In particular, a velocity range of −25 to 21 cm/yr was obtained from PSI-StaMPS, whereas a range of −30 to 25 cm/yr was obtained from the refined SBAS method. Upon computation of the vertical and east-west displacement components based on ascending and descending track data using both methods, deformation velocities of 51.5 and 52.5 cm/yr in the westerly direction on the western flank of Mount Etna were obtained from PSI-StaMPS and the refined SBAS method, respectively, whereas on the eastern flank, deformation toward the east was estimated to occur at a velocity of 50.1 or 54.2 cm/yr, respectively. PSI-StaMPS estimated a vertical deformation velocity of −5.3 to 18.3 cm/yr, whereas the refined SBAS method produced a velocity range of approximately −7 to 19 cm/yr. The interferogram obtained via Okada modeling showed two fault sources in the 2018 Mount Etna eruption and a total volume change of approximately $12.39 \times 106 \text{ m}^3$. From the modeling results, a lava flow prediction model was generated using the Q-LavHA program. The approaches described in this study can be used by government officials, authorities, and other decision-makers to monitor and assess the risk of volcanic activity in the region.

Key words: Mount Etna, PSI-StaMPS, refined SBAS, Okada model, Q-LavHA

Manuscript received June 21, 2022; Manuscript accepted September 14, 2022

*Corresponding author:
Chang-Wook Lee
Department of Science Education, Kangwon National University, 1 Gangwondaehakgil, Chuncheon-si, Gangwon-do 243341, Republic of Korea
Tel: +82-33-250-6731, Fax: +82-33-259-5600,
E-mail: cwlee@kangwon.ac.kr

1. INTRODUCTION

The activity levels of Mt. Etna, one of the most active volcanoes in the world, have continuously increased over the past 50 years (Clocchiatti et al., 2004). At 3324 m, Mount Etna is also the highest volcano in Europe (Neri et al., 2017). Due to the intensity of its eruptions, Mount Etna's volcanic activity should be monitored daily. Historical eruptions described the activities of Mount

Etna are increasing represented by intense eruptions and lava flows. In 1669, an eruption followed by lava production destroyed the villages surrounding Mount Etna, including parts of Catania City. The bigger eruption during 1991–1993 produced more lava flows than the 1669 eruption (Calvari et al., 1994). In the earlier 20th century, the 2001–2002 eruptions affected the tourist facilities and interrupted airport activities in Catania City. Furthermore, the eruptions caused economic losses of up to 800 million euros (Clocchiatti et al., 2004). One recent eruption in Mount Etna occurred in December 2018, starting with an increase in volcanic activity in July 2018 and a fissure eruption in August 2018. The eruption began on 24–27 December 2018 and was accompanied by a magnitude 4.9 earthquake near Catania City on 26 December 2018.

The development of radar satellites has made the analysis of volcanic activity much easier. For example, space-borne radar interferometry can be used to monitor volcanic deformation (Massonnet et al., 1995). Mount Etna was the first volcano mapped using satellite radar data, which revealed a sequence of deformations characterized by deflation during the end of the 1993 eruption (Lanari et al., 1998). Data on Mount Etna eruptions and the associated displacements can be used to explore the relationship between volcanism and volcanic instability (De Novellis et al., 2019). Given that several radar satellites are currently in operation, the amount of synthetic aperture radar (SAR) data available has also increased. With these data, a more advanced method for analyzing volcanic deformation using radar interferometry—the multi-interferogram framework—was developed. This method provides time-series measurements of a highly coherent target and overcomes most of the difficulty associated with unwrapping phases of interferometric synthetic aperture radar (InSAR) data from atmospheric noise using techniques such as Permanent/Persistent Scatterers Interferometry (PSI) (Ferretti et al., 2001; Hooper et al., 2004, 2012; Hooper and Zebker, 2007; Hooper, 2008) and small-baseline subset (SBAS) differential InSAR (DInSAR) analysis (Berardino et al., 2002; Lee et al., 2010, 2013; Lee, 2014). These methods provide more information on deformation events that occur on Mount Etna, significantly improving the insight of its structural setting (Bonforte et al., 2011).

According to recent research using DInSAR data, during the volcanic eruption on 24–27 December 2018, surface deformation of Mount Etna was detected (De Novellis et al., 2019). However, the study provided no time-series or multi-interferogram data covering the periods before, during, and after the eruption. Therefore, in this study, we applied the PSI-Stanford Method for Persistent Scatterers (StaMPS) and the refined SBAS DInSAR method to analyze Sentinel-1 SAR data from June 2018 to October 2019 to estimate deformation rates and gener-

ate a 1-year time series of Mount Etna spanning the December 2018 eruption period. We also ran a surface deformation simulation using the Okada model (Okada, 1985) to determine the volume of lava due to an eruption. Additionally, the Q-LavHA plugin was applied to produce a lava inundation probability simulation map (Mossoux et al., 2016).

2. MATERIALS AND METHODS

2.1. Study Area

Mount Etna is located on the island of Sicily, Italy, and has five active craters (Fig. 1): Voragine (VOR), the North-East Crater (NEC), Bocca Nuova (BN), the South-East Crater (SEC), and the New South-East Crater (Spampinato et al., 2019). One of the most famous areas on Mount Etna is Valle del Bove (VdB) (Fig. 1b), which is shaped like a horseshoe with an open eastern side. In the 24–27 December 2018 eruption, the lava flows produced by Mount Etna captured by Sentinel-2 satellite and unmanned Aerial Vehicles (UAVs) (De Beni et al., 2021) were moving southeast to Valle del Bove (Fig. 1b).

Mount Etna is among the most well-documented of all volcanoes, with information regarding its eruption dates recorded from 520–1270 BC (Branca and Del Carlo, 2004). The most destructive eruption occurred on 11 March 1669 and lasted until 11 July the same year. This eruption led to the formation of the sizable Monti Rossi composite cone after mutual explosions and effusive activities during the first three months, plus lava flows in the last month (Chester et al., 1986; Mulas et al., 2016). The total tephra fallout volume was approximately 8×10^7 m^3 from the 1669 eruption, equivalent to a Volcano Explosivity Index (VEI) of 2–3 (Behncke and Neri, 2003).

Over the last 20 years, Mount Etna erupted several times in various ways. The first flank eruption since the 1991–1993 eruption was produced on Mount Etna from July to August of 2001, and these eruptions mostly occurred on the south slope (Behncke and Neri, 2003). The next eruption of Mount Etna occurred in 2002 and lasted until 2003. This was the most massive eruption to date, with an estimated total mass of $4.4 \pm 0.6 \times 10^{10}$ kg, indicating a significant change in the volcano's dynamic regime (Neri et al., 2004, 2005, 2009; Andronico et al., 2008). The subsequent two eruptions occurred from 2004 to 2005 and in November 2006. With these eruptions, there was a change in eruption type, from an explosive event with extended fractures along the flanks preceded by intense seismic activity as in the 2001 and 2002–2003 eruptions, to a long-lasting effusive eruption with minor strombolian activity and few seismic precursors (Giacomoni et al., 2018). The eruptions involved a flank collapse, then affected the unstable eastern slope of the Southeast Crater (Corsaro,
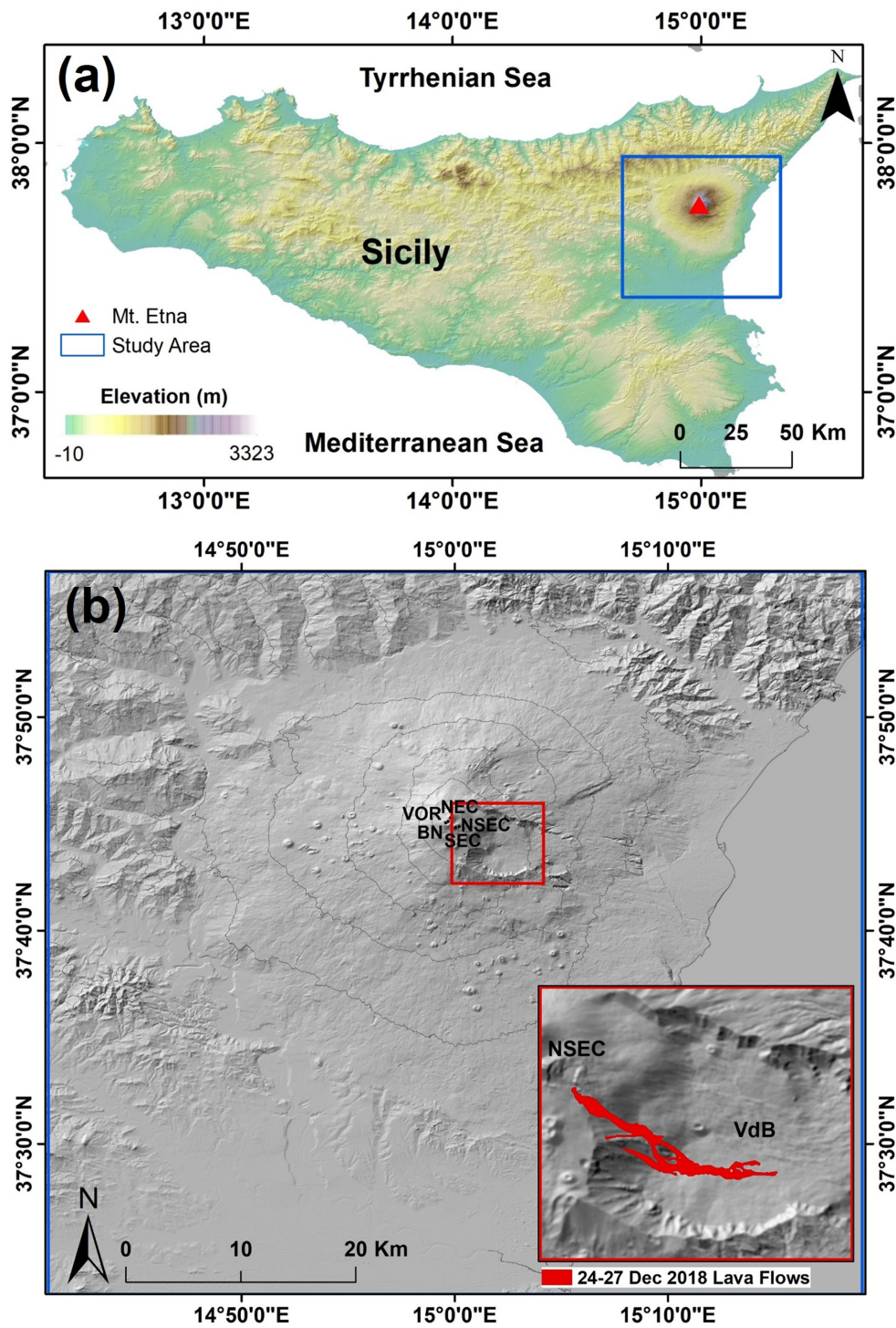
Fig. 1. (a) Location of Mt. Etna on Sicily Island, Italy, and the study area of the study shown in the blue box. (b) Shaded relief Shuttle Radar Topography Mission digital elevation model (DEM) shows the five active craters on Mt. Etna and lava flows of the 24–27 December 2018 eruption on the red box manually captured from Sentinel-2 image and De Beni et al. (2021). The five active craters are North-East Crater (NEC), New South-East Crater (NSEC), South-East Crater (SEC), Bocca Nuova (BN), and Voragine (VOR).

2005; Norini et al., 2009). In 2008–2009, a flank eruption commenced with several lava-fountaining episodes from March 2007. Based on GPS network data, the volcano underwent an inflation phase, generating a fracture from horizontal movement of up to 0.1 m and 0.2 m in vertical movement (Aloisi et al., 2009; Bonaccorso et al., 2011). Fourteen months after the start of continuous lava effusion, the eruption ended in July 2009. Since the 1991–1993 eruption, this has been the

longest flank eruption on Mount Etna. In January 2011, the Mount Etna summit crater was found to have increased with paroxysmal activity in the New Southeast Crater; a powerful lava fountain formed during the most intense phase, generating an eruption column that was several kilometers high (Giacomoni et al., 2018; Scollo et al., 2015). The peak of the eruptions occurred in early December 2015 with intense eruptive events across the entire summit crater (Corsaro et al., 2017). Since then, Mount Etna has produced eruptions of a similar type, those featuring paroxysmal activity—with variation in the crater location.

2.2. Dataset

This study used medium-wavelength (5.5 cm) Sentinel-1 SAR data (C-band) provided by the European Space Agency to simulate surface deformation associated with a volcanic eruption. The SAR data before, during, and after the December 2018 eruption are essential to provide precise information related to the activities of Mount Etna in the eruption period. A total of 56 datasets were acquired from June 2018 to October 2019 while the satellite was on the descending track (path 124) with VV polarization, whereas 34 datasets were acquired from the ascending track from August 2018 to October 2019. These data can be used to generate a surface deformation map associated with Mount Etna volcanic activity, and data were selected without consideration for seasonality or weather conditions.

2.3. Methods

A deformation map of Mount Etna was obtained using two time-series analysis methods, PSI-StaMPS (Hooper et al., 2004, 2012; Hooper, 2008)and a refined SBAS (Berardino et al., 2002; Lee et al., 2010, 2013). The further modeling analysis was performed using the Okada model (Okada, 1985) and Q-LavHA plugin (Mossoux et al., 2016), as detailed in the flowchart in Figure 2.

Sentinel-1 data from June 2018 to October 2019 were processed into InSAR data. If the data were to be processed for refined SBAS analysis, unwrapped DInSAR data would be used. Alternatively, if the data were to be processed for PSI-StaMPS analysis, wrapped DInSAR data phases would be used instead. The data were then analyzed using PSI-StaMPS and the refined SBAS method, and the results were compared. DInSAR data were also used to simulate surface deformation with the Okada model in determining the volume of lava from a given eruption, and Q-LavHA processing was carried out to generate a simulation map of lava inundation probability.
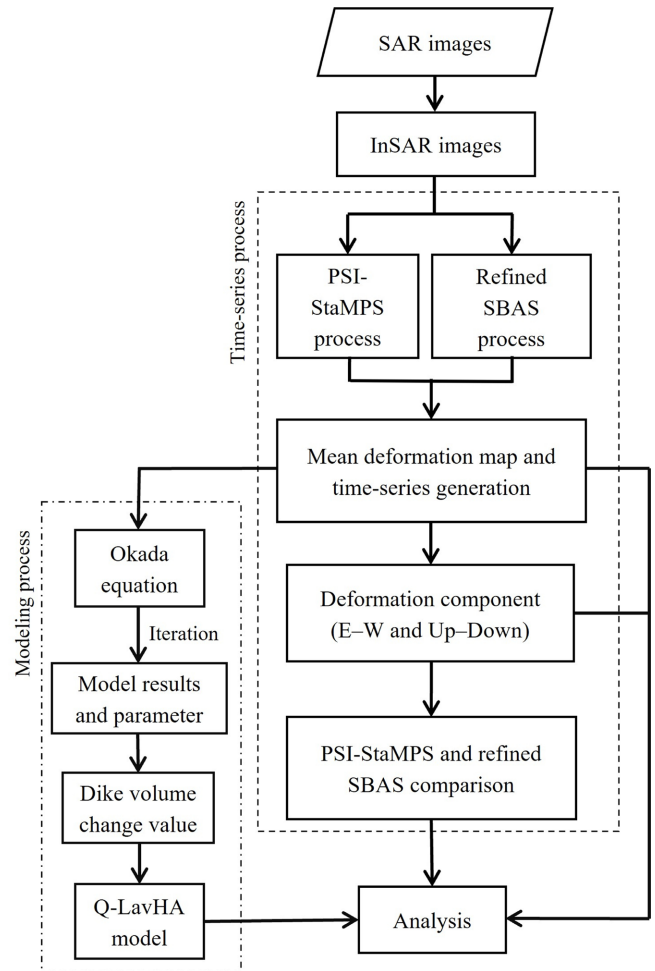

Fig. 2. The flowchart for generating the surface deformation and magma modeling was used in this study.

2.3.1. InSAR data processing

A two-pass interferometric approach was applied to SAR datasets that had already been acquired. Two SAR images obtained at different acquisition times were co-registered at sub-pixel accuracy to form an interferometric pair, with resampling of one image (slave image) performed such that it perfectly matched the other image (master image). The co-registered images were then cropped to generate an image that only contained the study area. An interferogram was generated from the image, and topographic phase contributions were subtracted based on 1-arcsec Shuttle Radar Topography Mission (SRTM) global data at 30-m resolution (topographic phase removal) to generate a DInSAR phase containing only the deformation phase (Zebker and Goldstein, 1985). This phase was then subjected to adaptive filtering to smooth the interferogram. The generated DInSAR phase subsequently underwent a phase-unwrapping procedure to generate an unwrapped DInSAR product.

2.3.2. Time-series interferometric processing

A time-series approach was used to observe displacements in the Mount Etna surface over time. PSI-StaMPS and the refined SBAS method were used to compare the first-order deformation rate. As pre-processing, a master-slave-pair dataset from DInSAR data were prepared as input for each algorithm. PSI-StaMPS uses a single master image, whereas the refined SBAS method uses several master images (Fig. 3).

2.3.3. PSI-StaMPS processing

The first method used to generate a deformation time series was StaMPS (Hooper et al., 2004, 2012; Hooper, 2008). The PSI-StaMPS flowchart modified from Sousa et al. (2011) is shown in Figure 4. This method is reliable for analyzing natural terrain because the deformation and interferometric phases are estimated to be spatially correlated. The method does not rely on assumptions

about the temporal nature of ground deformation.

A single reference (master) image was chosen from each of the ascending and descending tracks. Images on 4 and 22 March 2019 were selected to generate 33 and 55 interferograms for ascending and descending tracks, respectively (Fig. 3). All the generated data were then loaded into the StaMPS module. PSI-StaMPS selects the persistent scatterer using phase characteristics suitable for finding a low-amplitude natural target with phase stability (Hooper et al., 2004, 2012; Hooper and Zebker, 2007; Hooper, 2008). It also has an important advantage that the prior deformation model is not required (Crosetto et al., 2016). This process generates a deformation time series and estimates deformation velocity over the selected persistent scatterer.

2.3.4. Refined SBAS processing

Unlike the PSI-StaMPS method, SBAS processing prefers
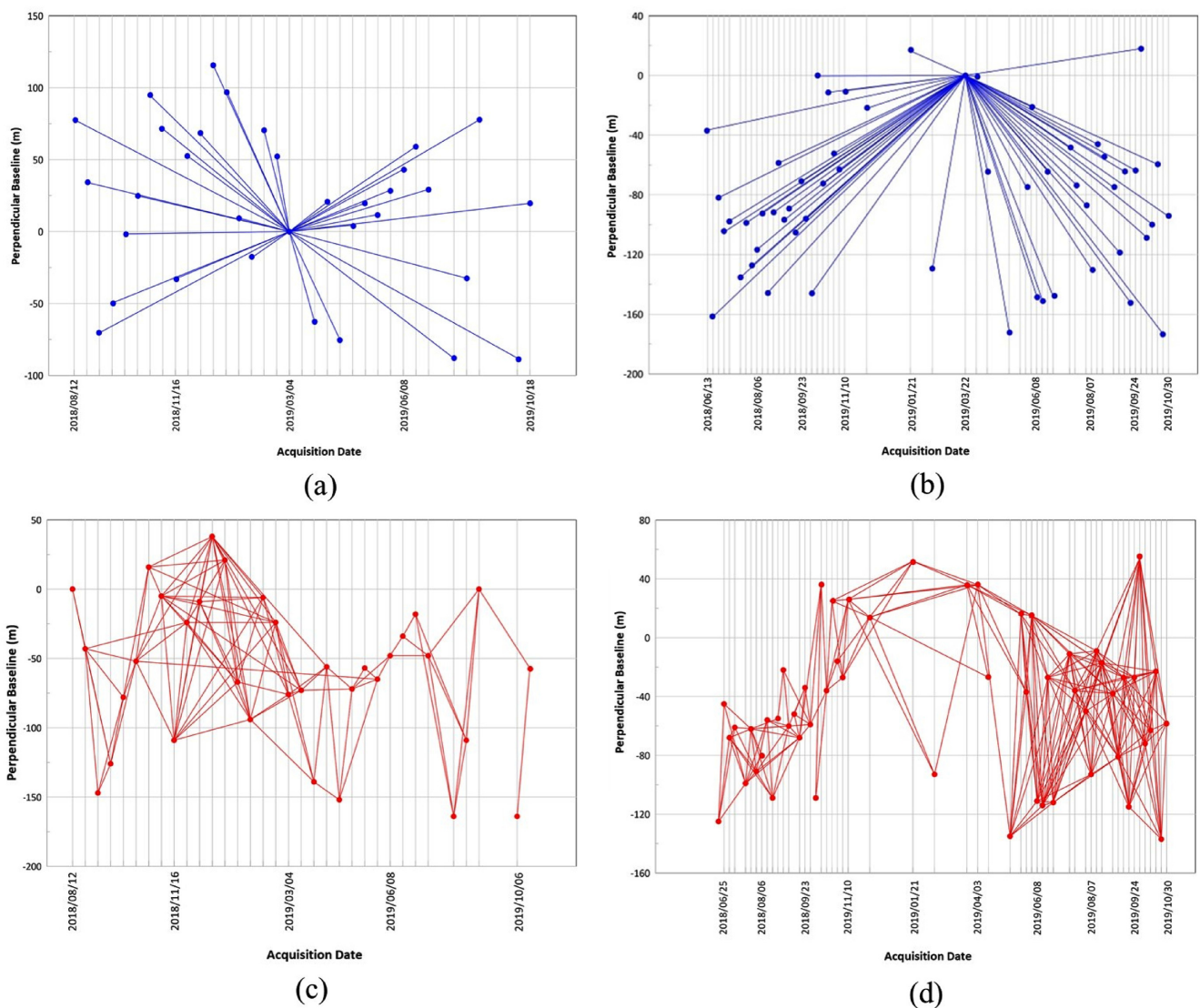

Fig. 3. Baseline graph showing PSI-StaMPS processing of (a) ascending and (b) descending track data and refined SBAS processing of (c) ascending and (d) descending track data.
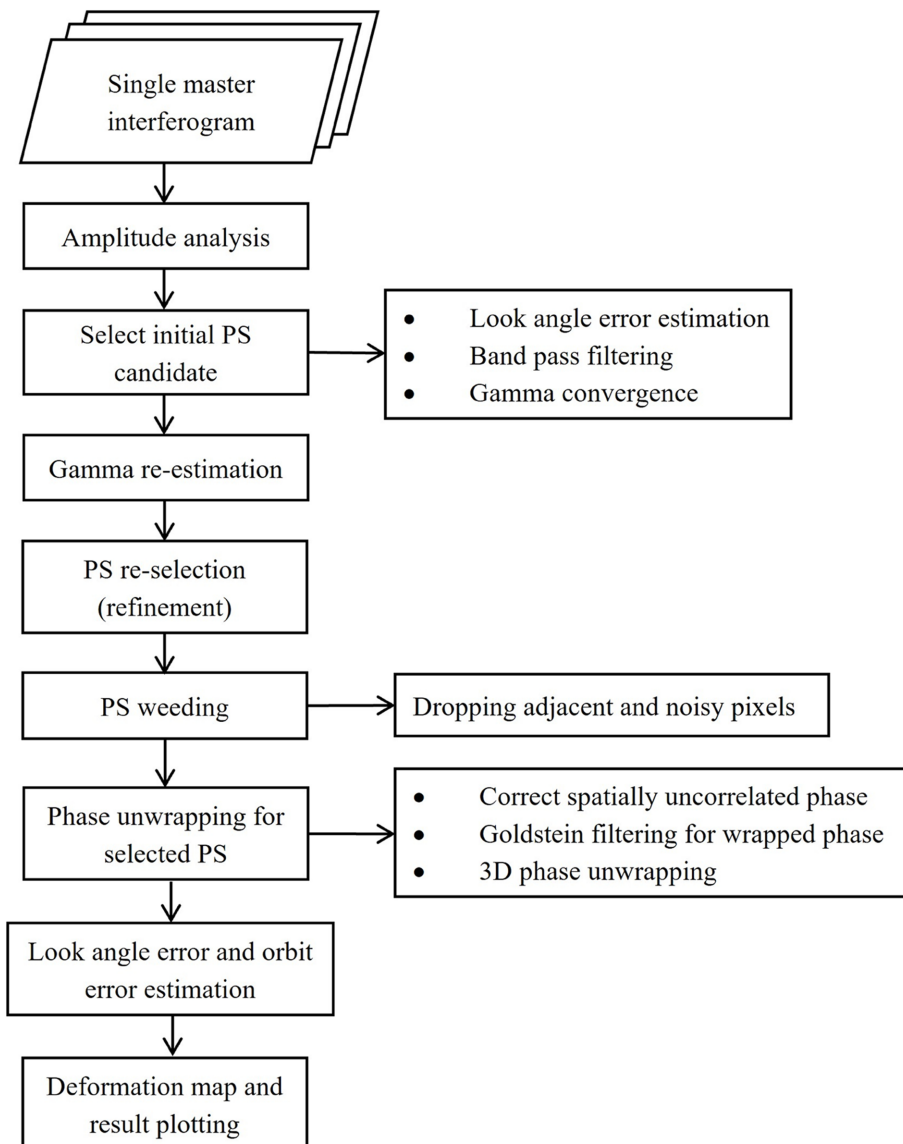
Fig. 4. The PSI-StaMPS flowchart (modified from Sousa et al., 2011). PS, persistent scatterer.

several master images to generate interferograms. Therefore, the SBAS method can employ more interferograms to generate time series and surface deformation maps than the PSI method. The SBAS algorithm used small baseline interferograms that overlap in time to reduce spatial decorrelation. The SBAS algorithm also mitigates the topographic error and atmospheric effect in interferometric pairs (Berardino et al., 2002). To obtain the best processing results, we only chose high-coherence interferograms with value of 0.6 (Hong and Wdowinski, 2011). After selecting a total of 339 high coherence interferograms (103 from ascending tracks and 236 from descending tracks (Fig. 3), surface deformation over time was calculated using the refined SBAS technique (Fig. 5).

This technique improves the accuracy of surface deformation estimation by reducing error factors such as topographic errors, atmospheric artifacts, unwrapping errors, and temporal noise

through multiple iteration processes (Lee et al., 2013). Any orbital error phase bias in the linear deformation rate is corrected using the residual interferogram. Meanwhile, atmospheric effects are specifically reduced using temporal high-pass and spatial low-pass filtering. This process generates a surface deformation time-series graph and a map of the estimated mean surface deformation over the study area.

2.3.5. Deformation components

In order to know the deformation characteristics more precisely, the horizontal and vertical components of deformation are retrieved by utilization of multi-satellite with different looking angle geometries (Pepe and Calò, 2017). The horizontal component is defined as East-West and North-South components, while the vertical component is the surface deformation in the Up-Down direction. However, the North-South components were
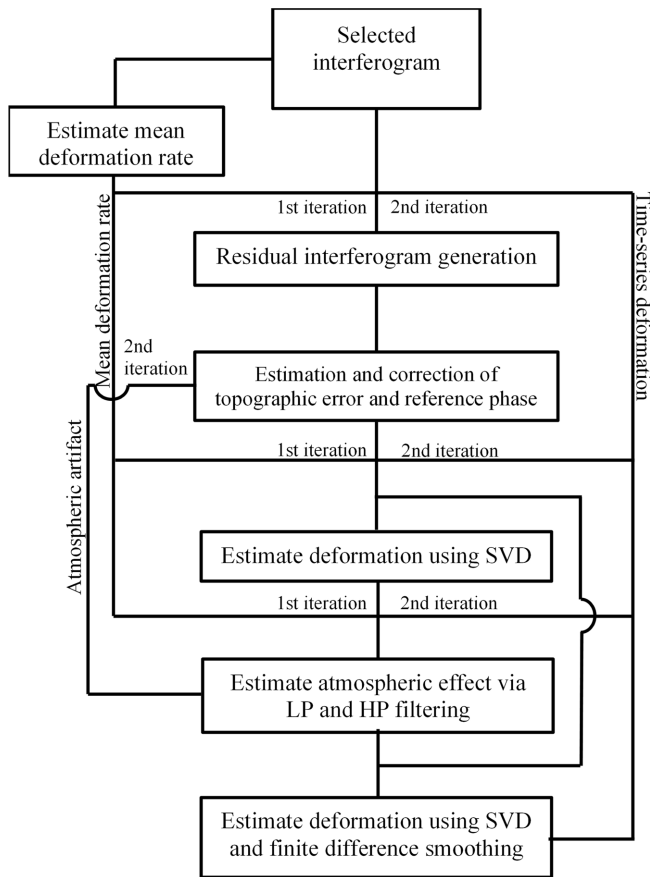
Fig. 5. The refined SBAS algorithm (modified from Lee et al., 2010). SVD, singular value decomposition; LP, low pass; HP, high pass.

considered to be ignored, given that the satellite azimuth direction is almost parallel to the North-South direction.

The East-West and vertical component is obtained by combining the InSAR data from two satellites (Pepe and Calò, 2017), ascending and descending satellites that have different side-looking angles, θ_1 and θ_2, respectively. The horizontal and vertical components symbolized as d_{E-W} and d_V, respectively, were generated by projecting the LOS deformation component d_{LOS} to the East-West and Up-Down according to Equation (1).

$$\begin{pmatrix} \sin\theta_1 & \cos\theta_1 \\ -\sin\theta_2 & \cos\theta_2 \end{pmatrix} \cdot \begin{pmatrix} d_{E-W} \\ d_V \end{pmatrix} = \begin{pmatrix} d_{LOS_1} \\ d_{LOS_2} \end{pmatrix}. \tag{1}$$

We simplified Equation (1) by using matrix calculation and assuming the side-looking angles of the ascending and descending satellites were equal to θ, as shown in Equation (2).

$$\begin{pmatrix} d_{E-W} \\ d_V \end{pmatrix} = \frac{\begin{pmatrix} d_{LOS_1}\cos\theta - d_{LOS_2}\cos\theta \\ d_{LOS_1}\sin\theta + d_{LOS_2}\sin\theta \end{pmatrix}}{\sin 2\theta} = \begin{pmatrix} \dfrac{d_{LOS_1} - d_{LOS_2}}{2\sin\theta} \\ \dfrac{d_{LOS_1} + d_{LOS_2}}{2\cos\theta} \end{pmatrix}. \tag{2}$$

The formula of Equation (2) explains that the East-West component is obtained from the difference between two LOS deformation components, while the vertical component is generated from the sum of the ascending and descending deformations. According to the formulas, we processed mean deformation from the result of ascending track and descending track data to produce deformation components on Mount Etna.

2.3.6. Modeling

A deformation model was generated using the Okada equation to calculate an analytical solution of surface deformation caused by the activities of shear and tensile faults in elastic half-space (Okada, 1985). This model is widely used to simulate ground deformation from local perturbation such as magmatic intrusion from volcanic dikes and earthquake-associated tectonic fault activity (Fadhillah et al., 2022). A two-step nonlinear and linear optimization approach was used to run the model (Wright et al., 2003; De Novellis et al., 2019). The nonlinear optimization defined rupture mechanisms and the fault geometry based on the Levemberg-Marquardt algorithm (Marquardt, 1963) and a linear inversion used to obtain the opening distribution with Monte Carlo restarts while avoiding local minima (Wright et al., 1999). A three-dimensional displacement vector was projected into the satellite line of sight (LOS) to obtain the modeled results. The model was subsequently applied to analyze the earthquake and the source of the 2018 eruption. The latest research indicated that there were two sources of the 2018 eruption beneath Mount Etna (Bonforte et al., 2019; De Novellis et al., 2019). Thus, the model that was generated in this study also included two sources. The model used the mean deformation map derived from SBAS processing of descending track data because more data could be provided for each pixel, and the process of model generation could be simplified.

After the model with the best outcome (based on the residual phases generated) was identified, Q-LavHA processing was carried out to simulate the lava flow (Mossoux et al., 2016). The TINITALY DEM by Tarquini et al. (2007) with the 10-meter resolution was used as input data in simulating lava flows using Q-LavHA based on a FLOWGO method. The fill tool in ArcMap was used to fill the sink or depression in the DEM that can cause lava flows to stop while simulating (Hakim et al., 2022). In simulating lava flows using the Q-LavHa plugin, the DEM quality and selected parameters affect the simulation results (Mossoux et al., 2016). The vent locations of the 2018 December fissure eruption were estimated according to the actual lava flow map generated by De Beni et al. (2021) and observed the optical imagery. Then, the lava inundation probability was estimated according to the pre-selected linear eruptive sources as follows:

$$\text{prob}_i = \frac{1}{\text{total number of iterations}}, \tag{3}$$

$$\text{PROBi} = \frac{\Sigma \text{prob}_i}{\text{number of vents simulated}} \times \varphi \times p_{susc}, \tag{4}$$

where PROB_i is the probability that the final pixel would be inundated, φ is the probability of reaching a certain length, and p_{suse} is the probability that the vent from which the flow line starts would occur at a particular location. In this study, the one-dimensional FLOWGO cooling-limited model was used to define the Lava flow length constraints (Harris and Rowland, 2001). The input of effusion rate was assumed as the total change of dike volume derived from the Okada model divided by the December 2018 eruption period. The utilization of the FLOWGO model for lava flow simulation requires corrective factors and parameters that describe the physical and chemical characteristics of the Etna's lava flows. The corrective factors, the lava thickness parameter, are needed to overcome topographic obstacles and pits when generating propagation of lava flows. The minimum and maximum lava thickness of the December 2018 eruption were set from 0.1 m to 9.1 m (De Beni et al., 2021). Meanwhile, the physical and chemical parameters are presented in Table 1.

The Q-LavHA results were compared with actual lava flows to get the accuracy assessment of the lava flow simulation. The results from the Q-LavHA analysis were compared with actual lava flow data captured by Sentinel-2 images after the eruption, supported by the existing lava flow map (De Beni et al., 2021). The fitness indexes (FI), which consist of the true-positive (TP) rate, false-positif (FP) rate, and false-negative (FN) rate, were

Table 1. The parameters used for Etna's lava flow simulation using Q-LavHA with the FLOWGO method

FLOWGO Parameter (Unit)	Symbol	Values	Sources
Channel width-depth ratio	w/r	6.19	Mossoux et al. (2016)
Thermal Parameters			
Eruption temperature (°C)	T_{erupt}	1100	Cordonnier et al. (2015)
Crust temperature (°C)	T_{crust}	150	Mossoux et al. (2016)
Offset (°C)	$T_{erupt} - T_{core}$	500	Mossoux et al. (2016)
Thermal conductivity constant	d	−0.00756	Mossoux et al. (2016)
Viscosity and Elasticity			
Lava initial viscosity (Pa·s)	η	3766.76	Mossoux et al. (2016)
a constant (1/K)	a	0.04	Dragoni (1989)
b constant (Pa)	b	0.01	Dragoni (1989)
c constant (1/K)	c	0.08	Dragoni (1989)
Convection Parameters			
Wind speed (m/s)	U	5	Harris and Rowland (2001)
$\dfrac{\text{Friction windspeed}}{\text{wind speed}^2}$	C_h	0.0036	Harris and Rowland (2001)
Air temperature (°C)	T_{air}	25	Rodriguez-Gonzalez et al. (2021)
Air density (kg/m³)	ρ_{air}	0.4412	Harris and Rowland (2001)
Air specific heat capacity (J/kgK)	cp_{air}	1200	Cordonnier et al. (2015)
Velocity Constant			
Gravity (m/s²)	g	9.18	Constant for earth
Crystal Parameters			
Initial phenocryst mass fraction	Φ_{phen}	0.3	Mossoux et al. (2016)
Growth rate	df/dT	0.005	Mossoux et al. (2016)
Latent heat of crystallization (J/kg)	L	3.5×10^5	Amato et al. (2021)
Inverse of maximum crystal concentration	R	1.51	Harris and Rowland (2015)
Lava Density and Vesicularity			
Dense-rock equivalent density (kg/m³)	ρ_{DRE}	2600	Amato et al. (2021)
Vesicularity (%)	Φ_b	22	Harris and Rowland (2015)
Radiation Parameters			
Stephan Boltzmann constant (W/m²K⁴)	σ	5.67×10^{-8}	Mossoux et al. (2016)
Emissivity of basalt	ε	0.95	Rodriguez-Gonzalez et al. (2021)
Conduction Parameters			
Thickness of lava crust (%)	H_b	19	Harris and Rowland (2001)
T (base of lava crust) (°C)	T_{base}	500	Harris and Rowland (2001)
Lava thermal conductivity (W/mK)	k_{lava}	2	Mossoux et al. (2016)

used to measure the accuracy of the simulation results (Mossoux et al., 2016). The true-positive rate assesses the overlapped area of an actual lava flow and a simulated flow. The false-negative rate was used to assess the mismatch between simulated flow and actual flow due to underestimation. Meanwhile, the false-positive (FP) rate was used to assess mismatch due to overestimation. The formulas used are as follows:

$$FI_{\text{true-positive}} = \frac{A_S \cap A_r}{A_S \cup A_r}, \qquad (5)$$

$$FI_{\text{false-positive}} = \frac{A_s - (A_S \cap A_r)}{A_S \cup A_r}, \qquad (6)$$

$$FI_{\text{false-negative}} = \frac{A_s - (A_S \cap A_r)}{A_S \cup A_r}, \qquad (7)$$

where A_s indicates the area covered by the simulated lava flow, and A_r symbolizes the area covered by the actual lava flows (Mossoux et al., 2016). The FI varies between zero and one. These values are important for properly interpreting simulation results so that they can be used effectively in risk management.

3. RESULTS

3.1. Results of Time-series Analysis

The mean surface deformation and time-series deformation results using PSI-StaMPS and the refined SBAS method are shown in Figure 6. Time-series results were obtained for two pre-selected points on Mount Etna. Mean surface deformation velocity maps of the Mount Etna area generated using PSI-StaMPS and the refined SBAS method with data from ascending and descending tracks are shown in Figures 6a–d.

Figures 6a–b show the results of PSI-StaMPS analysis from both tracks for two different selected points, P1 and P2, which indicated activity due to surface deformation on the western (P1) and eastern (P2) flanks of the volcano during the eruption period. According to the analysis of ascending track data, the mean deformation velocity at P1 on the western flank moving toward the satellite LOS was 21 cm/yr, whereas that at P2 on the eastern flank moving away from the satellite LOS was 25 cm/yr. Based on descending track data, the mean deformation velocities at P1 and P2 had inverted directions relative to those based on ascending track data, with respective velocities of 20 cm/yr moving away from the satellite LOS and 16 cm/yr moving toward the satellite LOS. The deformation time-series graphs produced by PSI-StaMPS showed that deformation mostly occurred after the eruption on 27 December 2018 at both points. The total deformation distances based on ascending track data were ~25 cm moving

toward the satellite LOS at P1 and ~15 cm moving away from the satellite LOS at P2 (Figs. 6e and f). Opposite to ascending track results, descending track data (Figs. 6g and h) show the total deformation distances of ~20 cm moving away from the satellite LOS at P1 and ~20 cm moving toward the satellite LOS at P2.

Meanwhile, comparable results to PSI-StaMPS were obtained by the refined SBAS method (Figs. 6c and d). Similar deformation directions as with PSI-StaMPS were obtained for P1 and P2 using data from both tracks. Nevertheless, differences in values between the two methods were noted. Based on ascending track data, the mean surface deformation velocities at P1 and P2 were approximately 20 and 30 cm/yr, respectively, whereas the descending track data resulted in the respective values being approximately 22 and 23 cm/yr. The total deformation distances at P1 and P2 based on ascending track data were approximately 25 and 20 cm, respectively (Figs. 6e and f), whereas those based on descending track data were approximately 18 and 20 cm, respectively (Figs. 6g and h). The deformation pattern on Mount Etna was considered related to the large dike intrusion that occurred in the December 2018 eruption. This intrusion opened fissure eruption and caused the deformation in the opposite direction on the eastern and western flanks of Mount Etna (Bonforte et al., 2019).

3.2. Deformation Component

The previously obtained surface deformation results were calculated based on the LOS direction. Elucidating the degree of deformation along several directions would provide more information. The degree of deformation can be calculated by combining data from ascending and descending tracks in multi-temporal interferometric analysis (Pepe and Calò, 2017). The results of such analysis shown in Figure 7 reveal that the deformation in the 2018 Mount Etna eruption primarily occurred along an east-west direction with P1 moving approximately 51.5 and 52.5 cm westward according to PSI-StaMPS and the refined SBAS method, respectively, and P2 moving approximately 50.1 and 54.2 cm eastward, respectively. Vertical deformation also occurred with subsidence in some northern and southern parts of Mount Etna, whereas deformation along the direction of subsidence was observed in the eastern and western parts. In the La Montagnola area (outlined in red in Figs. 7c and d), subsidence of 6.2 cm was predicted by PSI-StaMPS, whereas 12.3 cm of subsidence with deformation was predicted using the refined SBAS method.

There were some differences between the results from both analyses. Since PSI-StaMPS can only choose a stable scatterer through the selection process, several points with no data were obtained.
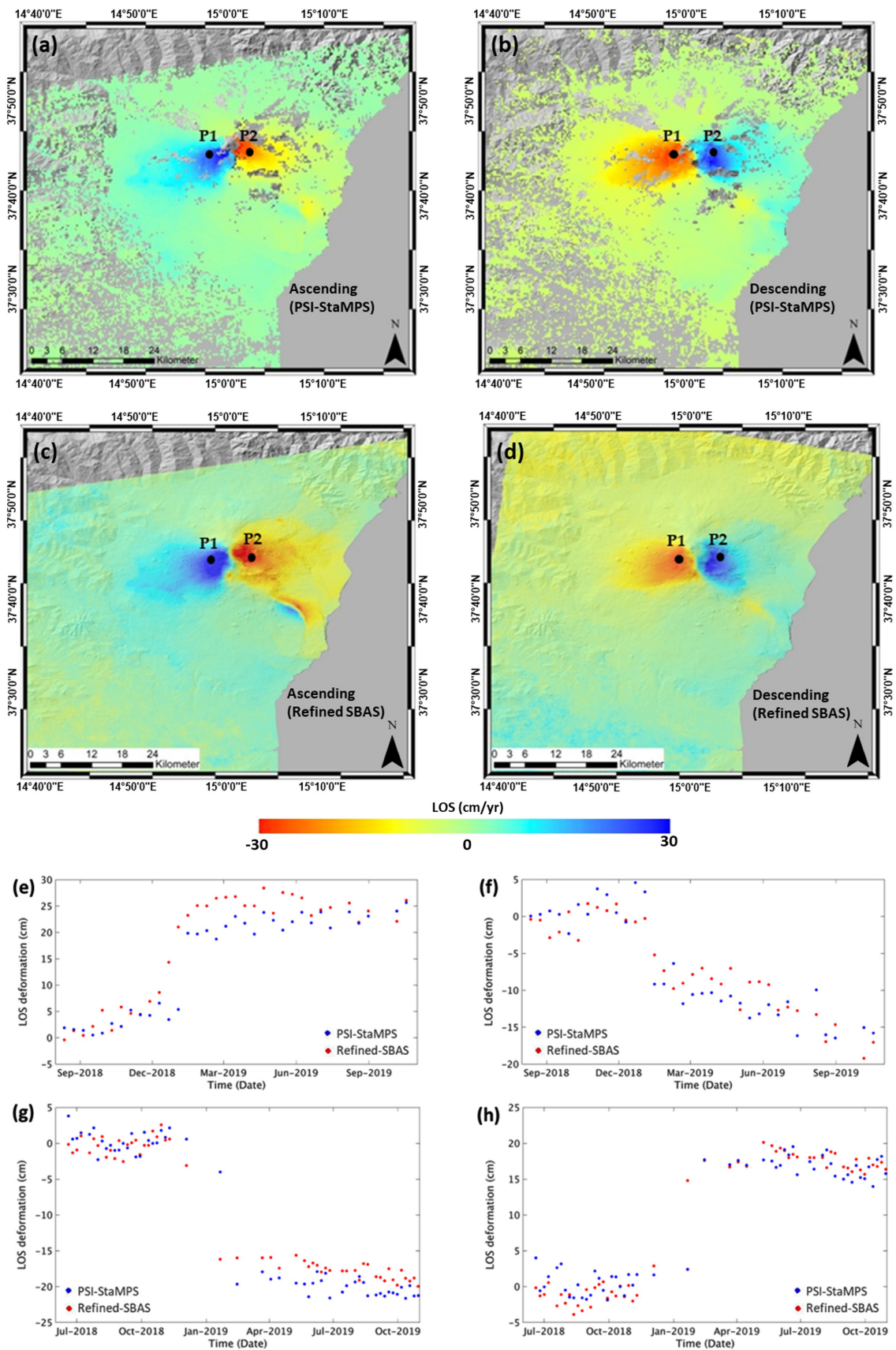
Fig. 6. Mean deformation velocity maps were generated using PSI-StaMPS with (a) ascending and (b) descending track data and the refined SBAS method with (c) ascending and (d) descending track data. Line-of-sight (LOS) deformation time series from PSI-StaMPS and the refined SBAS method based on ascending track data for points (e) P1 and (f) P2 and descending track data for points (g) P1 and (h) P2.
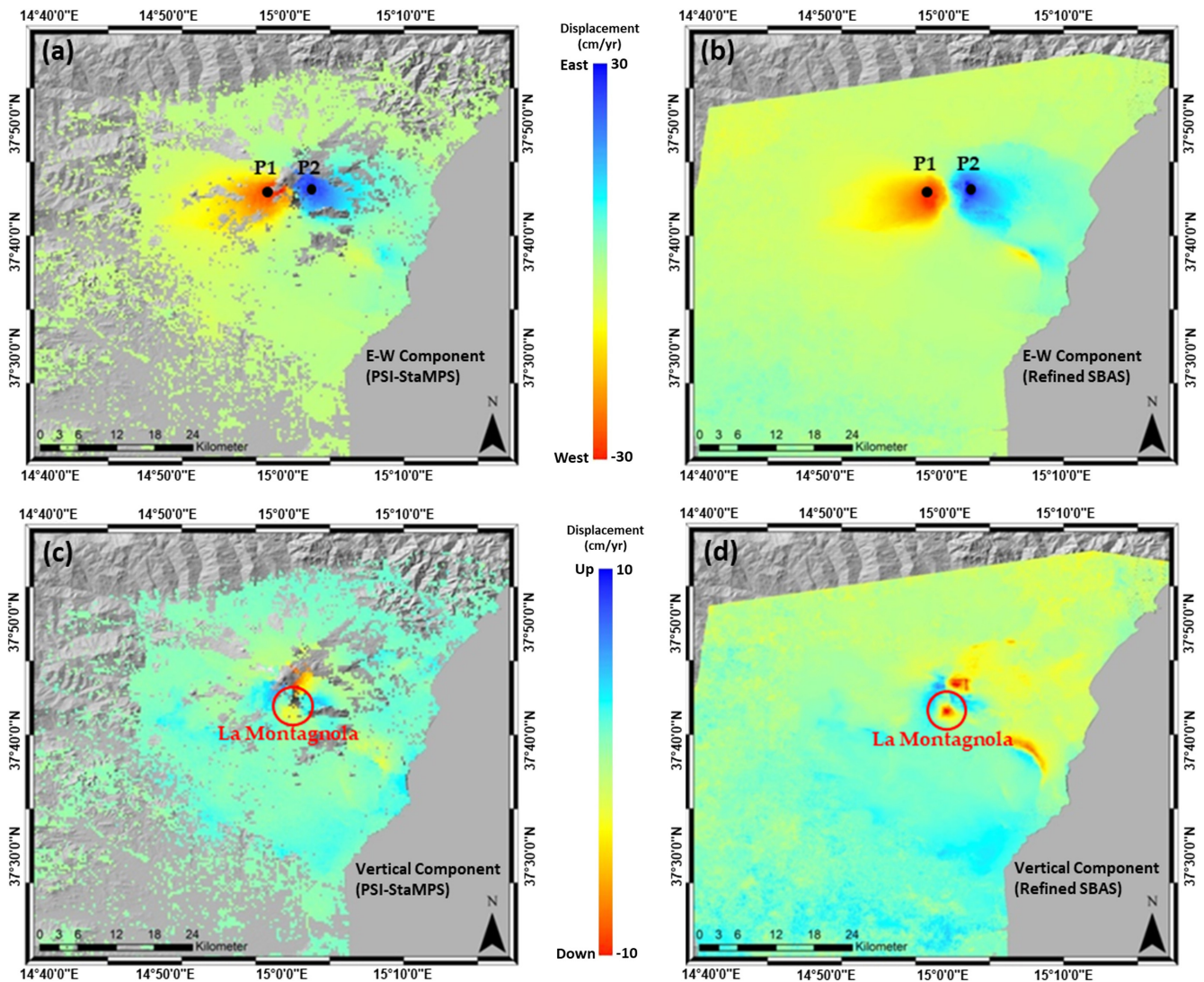
Fig. 7. Degree of east-west displacement according to (a) PSI-StaMPS and (b) refined SBAS analysis. Degree of vertical displacement according to (c) PSI-StaMPS and (d) refined SBAS analysis. The La Montagnola area is outlined in red in (c) and (d).

3.3. Modeling Results

The Okada model using a two-step approach involving linear and nonlinear optimization successfully simulated the 2018 Mount Etna eruption as shown in Figure 8.

The synthetic interferogram shows two Okada sources consisting of shallow and deep dikes below eruptive vents. Similarly, two shallow and deep sources (Okada sources) were observed in the earthquake area (Fig. 8b), with source parameters listed in Table 2. We obtained most of the retrieved signals of deformation properly, as can be seen from the residual interferogram displaying clear data (Fig. 8c). The residual interferogram was generated by subtracting the real interferogram (Fig. 8a) from the synthetic interferogram. The parameters used for this model are listed in Table 2.

A shallow source of 2 km in length and 0.57 km in width extended from the summit area to the south of the deep source. The slip/opening was approximately 1.2 m with a dip of 61°, and the volume of the dike was 1.37×10^6 m³. The deep source extended southeastward and had 3.8 km in length, 1 km in width, and an opening of ~2.9 m. The volume of the dike was 11.02×10^6 m³. The total volume change due to both Okada sources was approximately 12.39×10^6 m³ (0.001239 km³), which corresponds to a VEI of ~3 (Newhall et al., 2018; Achmad et al., 2020).

The lava flow simulation generated using Q-LavHA showed that the probable lava flow was similar to the actual lava flow observed using Sentinel-2 optical imagery obtained on 29 December 2018 (outlined in blue in Fig. 9a). Pixels containing actual lava were exported in a raster image after manual selection (Fig. 9b). The Q-LavHA results were visualized using the FLOWGO model provided as a plugin (Fig. 9c).
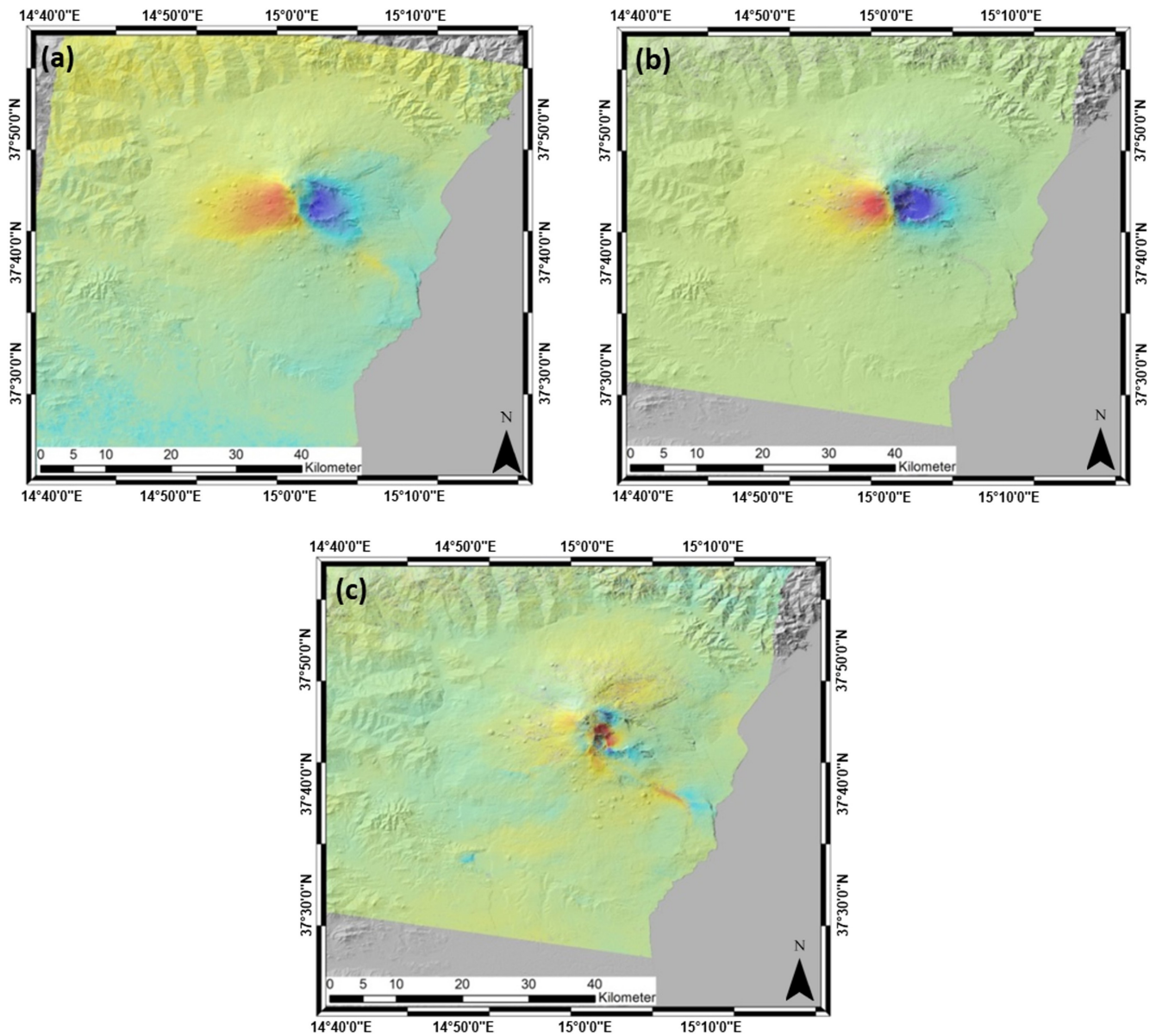
Fig. 8. LOS-projected deformation maps are based on (a) original data, (b) the results of modeling, and (c) residual data.

Table 2. Source parameters of the 2018 Mount Etna eruption

Parameter	Shallow	Deep
Length (km)	2	3.8
Width (km)	0.57	1
Depth (km)	0.5	1.73
Dip (°)	61	70
Strike (°)	356	347
Slip/opening (m)	1.2	2.9

The total dike volume acquired from the Okada model was used in the Q-LavHA analysis as an input of the effusion rate. We assumed simply that the entire dike load consisted of lava during the period of the eruption. The results were compared with actual lava flow data derived from Sentinel-2 optical images

taken on 29 December 2018 and a related lava map (De Beni et al., 2021), and assessed the accuracy based on the FI. In the comparison of simulated lava flow with the actual lava flow outline, the TP rate was 0.46, FP rate was 0.38 and the FN rate was 0.16.

4. DISCUSSIONS

4.1. Comparison of Time Series Generated using PSI-STAMPS and the Refined SBAS Method

The PSI-StaMPS results were more affected by noise, whereas the refined SBAS method imposes spatial and temporal constraints on the interferogram selection to mitigate noise. In terms of the
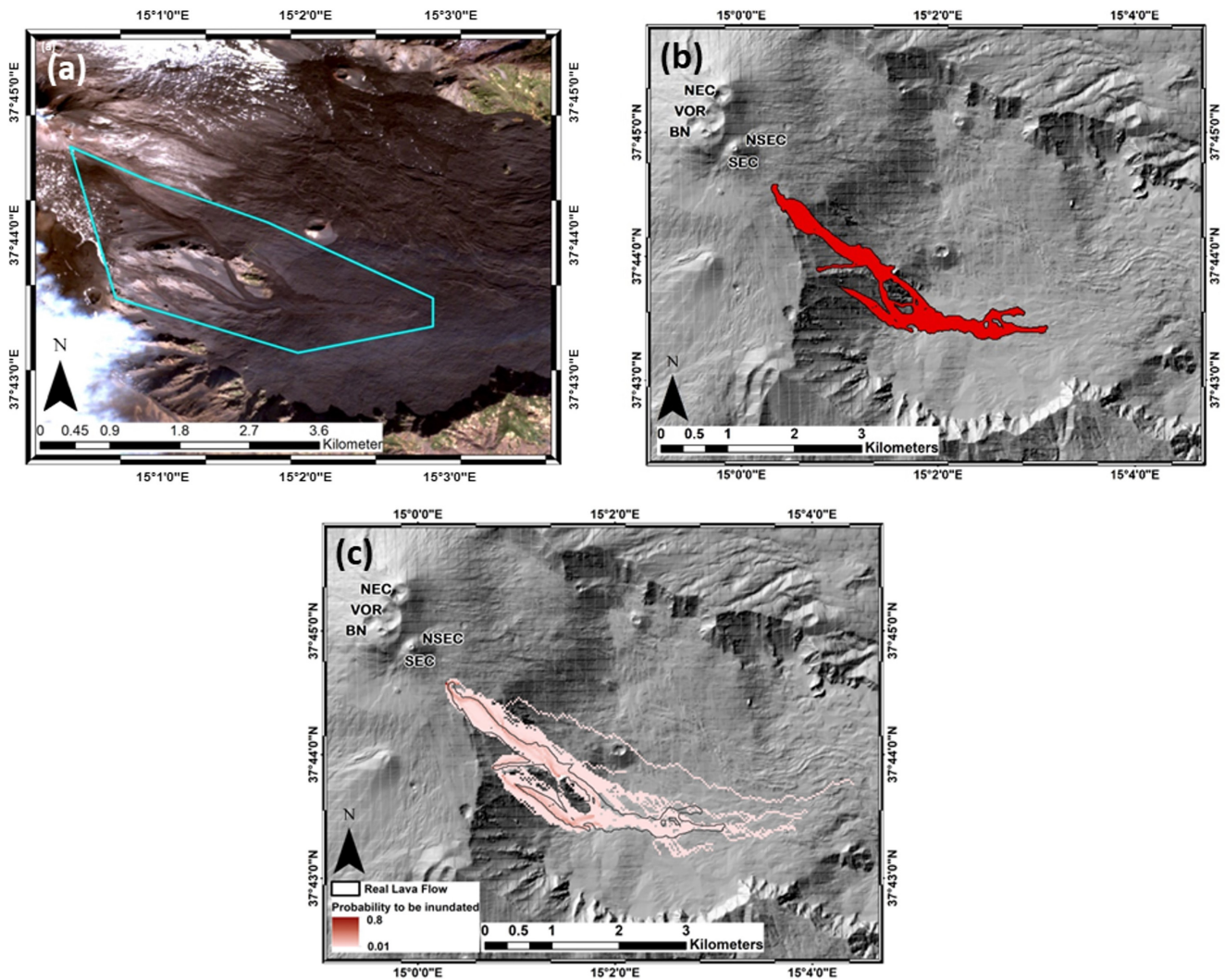
Fig. 9. (a) Sentinel-2 natural-color image of actual lava flow captured on 29 December 2018. (b) Pixels correspond to lava flow after the December 2018 eruption and are depicted in a shaded relief DEM generated from Sentinel-2 image and related lava flow map provided by De Beni et al. (2021). (c) Lava inundation probabilities over the volcano surface after the 2018 eruption.

deformation time series at a given point, the refined SBAS time series exhibited a clearer trend curve than the PSI-StaMPS time series. From a scatterplot, the results from both PSI-StaMPS and the refined SBAS method exhibited good agreement, with a coefficient of determination (R^2) of approximately 0.8 (Fig. 10).

This result was also confirmed in a previous study that compared the PSI and SBAS techniques in a case of land subsidence in Bucharest, Romania (Gheorghe and Armaş, 2016). The method by which radar targets being the main difference between PSI and SBAS techniques are selected, whether reliable phase measurements are taken when using the same SAR images. The PSI-StaMPS selects a persistent scatterer (PS) in generating surface deformation, while the SBAS prefers the distributed scatterer (DS). Technically, the PSI-StaMPS uses a master image to which all other acquisitions are referenced, whereas the SBAS prefers

appropriate master-slave pairs with geometric and temporal baselines that maximize coherence. Because the method uses persistent scatterers, the PSI-StaMPS observation area is much smaller than the actual pixel resolution of the radar instrument. As such, the baseline decorrelation does not affect the scatterers, and very long baseline interferograms can be used to build time series (Osmanoğlu et al., 2016).

On the other hand, the SBAS method can be affected by baseline decorrelation, with this more likely to occur in non-urban areas. Thus, the original SBAS algorithm was enhanced to produce the refined SBAS algorithm by suppressing errors related to temporal decorrelation and other noises, improving estimates of atmospheric artifacts, setting specific reference points, and improving linear deformation rate estimates by avoiding phase-unwrapping errors (Lee et al., 2010; Lu and Dzurisin, 2014;
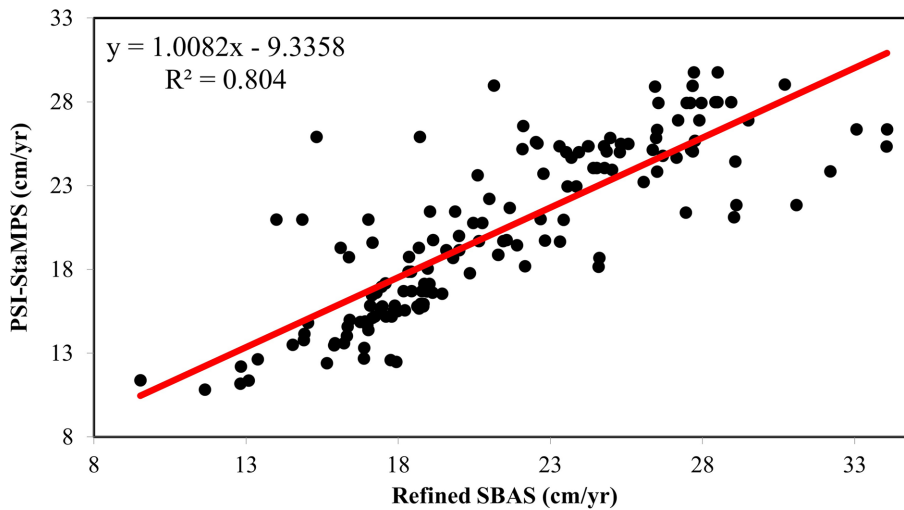
Fig. 10. Comparison of mean deformation velocities derived using the refined SBAS method and PSI-StaMPS.

Osmanoğlu et al., 2016). This technique reduces the number of error factors over several processing iterations, improves the accuracy of surface deformation estimations, and decreases interferogram noise. Although these methods are different, the time-series trend was similar, with an R^2 of ~0.8. Thus, the time series generated using the refined SBAS method can be considered valid.

4.2. Okada and Q-LavHA Modeling

The first Okada source, a deep and wide dike below the eruptive vents, was able to produce much denser deformation signals on the summit area and affect the whole volcanic edifice. The second Okada source, a shallow and small dike, only had a moderate effect due to its narrow width. Based on the modeling results, we can assume that the eruption process on Mount Etna was driven by magma that moved upwards and intruded into the deep dike (first Okada source). This eruption system is similar to the eruption in 2001 (Coltelli et al., 2007). After the magma intruded into the deep dike, it moved into the smaller and shallower dike, thus cutting through the volcano edifice, but with a smaller effect. Similar findings were obtained from Q-LavHA modeling. The Q-LavHA modeling results were associated with a TP rate of 0.46, an FP rate of 0.38, and an FN rate of 0.16. Figure 9c represents that the actual lava flow matches the simulated lava. TP rate represents 46% parts of actual lava simulated well, and the main channel of the lava flow has a high probability of being inundated. The FP rate shows some overestimation which was relatively high, and causing a low TP rate. Our model estimated the effusion rate by dividing the dike volume and the eruption period. This model assumed the dike intrusion load was entirely lava during the eruption period affecting the simulation result. However, the high overestimation with

low inundation probability is not an obstacle in hazard assessment study (Rodriguez-Gonzalez et al., 2021). Meanwhile, the FN rate was lower than other fitness indexes, which indicates the model rarely underestimated the lava flow area. Thus, most of the actual lava flow area was appropriately simulated, and the result can be utilized for hazard assessment purposes.

5. CONCLUSIONS

This work showed that PSI-StaMPS and the refined SBAS approach are suitable for analyzing volcanic eruption data. Both methods are cost-effective and can provide helpful information for managers responsible for volcanic hazard mitigation. There were some differences in the results obtained from PSI-StaMPS and the refined SBAS technique. The velocity range according to PSI-StaMPS was −25 to 21 cm/yr, whereas that according to the SBAS method was −30 to 25 cm/yr. These differences can be estimated come from the scattering characteristics of the ground surface and PSI-StaMPS being optimized for cells dominated by a single scatterer in contrast to the refined SBAS method, which focuses on distributed scatterers (no dominant element across cells). Additionally, the latter method is more sensitive to temporal and volume decorrelations.

According to modeling analysis, the two Okada sources in this eruption consist of shallow and deep dikes. The shallow dike had a length of 2-km, a width of 0.57-km, a slip/opening of ~1.2 m, a dip of 61^0, and a volume of 1.37×10^6 m^3. The second Okada source is a deep dike with an approximate length of 3.8 km and width of 1 km, an opening of 2.9 m, and a volume of 11.02×10^6 m^3. The Q-LavHA results were associated with an TP rate of 0.46, an FP rate of 0.38, and an FN rate of 0.16 from assessing the FI between simulation results and actual lava flow captured by Sentinel-2 optical images taken on 29 December

2018 and related lava flow map provided by De Beni et al. (2021). Thus, the approach described in this study can be used by government officials, authorities, and other decision-makers to monitor volcanic activity for risk assessment purposes.

ACKNOWLEDGMENTS

REFERENCES

Achmad, A.R., Lee, S., Park, S., Eom, J., and Lee, C.W., 2020, Estimating the potential risk of the Mt. Baekdu Volcano using a synthetic interferogram and the LAHARZ inundation zone. Geosciences Journal, 24, 755–768. https://doi.org/10.1007/s12303-020-0032-9

Aloisi, M., Bonaccorso, A., Cannavò, F., Gambino, S., Mattia, M., Puglisi, G., and Boschi, E., 2009, A new dyke intrusion style for the Mount Etna May 2008 eruption modelled through continuous tilt and GPS data. Terra Nova, 21, 316–321. https://doi.org/10.1111/j.1365-3121.2009.00889.x

Amato, E., Corradino, C., Torrisi, F., and Del Negro, C., 2021, Mapping lava flows at Etna Volcano using Google Earth Engine, open-access satellite data, and machine learning. International Conference on Electrical, Computer, Communications and Mechatronics Engineering (ICECCME) 2021, Mauritius, Oct., 7–8. https://doi.org/10.1109/ICECCME52200.2021.9591110

Andronico, D., Scollo, S., Caruso, S., and Cristaldi, A., 2008, The 2002–03 Etna explosive activity: tephra dispersal and features of the deposits. Journal of Geophysical Research, 113, B04209. https://doi.org/10.1029/2007JB005126

Behncke, B. and Neri, M., 2003, The July–August 2001 eruption of Mt. Etna (Sicily). Bulletin of Volcanology, 65, 461–476. https://doi.org/10.1007/s00445-003-0274-1

Berardino, P., Fornaro, G., Lanari, R., and Sansosti, E., 2002, A new algorithm for surface deformation monitoring based on small baseline differential SAR interferograms. IEEE Transactions on Geoscience and Remote Sensing, 40, 2375–2383. https://doi.org/10.1109/TGRS.2002.803792

Bonaccorso, A., Bonforte, A., Calvari, S., Del Negro, C., Di Grazia, G., Ganci, G., Neri, M., Vicari, A., and Boschi, E., 2011, The initial phases of the 2008–2009 Mount Etna eruption: a multidisciplinary approach for hazard assessment. Journal of Geophysical Research: Solid Earth, 116, B03203. https://doi.org/10.1029/2010JB007906

Bonforte, A., Guglielmino, F., Coltelli, M., Ferretti, A., and Puglisi, G., 2011, Structural assessment of Mount Etna volcano from permanent scatterers analysis. Geochemistry, Geophysics, Geosystems, 12, Q02002. https://doi.org/10.1029/2010GC003213

Bonforte, A., Guglielmino, F., and Puglisi, G., 2019, Large dyke intrusion and small eruption: the December 24, 2018 Mt. Etna eruption

imaged by Sentinel-1 data. Terra Nova, 31, 405–412. https://doi.org/10.1111/ter.12403

Branca, S. and Del Carlo, P., 2004, Eruptions of Mt. Etna during the past 3,200 Years: a revised compilation integrating the historical and stratigraphic records. In: Bonnacorso, A., Calvari, S., Coltelli, M., Del Negro, C., and Falsaperla, S. (eds.), Mt. Etna: Volcano Laboratory. Geophysical Monograph Series, 143, p. 1–27. https://doi.org/10.1029/143GM02

Calvari, S., Coltelli, M., Neri, M., Pimpilo, M., and Scribano, V., 1994, The 1991–1993 Etna eruption: chronology and lava. Acta Vulcanologia, 4, 1–14.

Chester, D.K., Duncan, A.M., Guest, J.E., and Kilburn, C.R.J., 1985, Mount Etna?: The Anatomy of a Volcano. Springer, Dordrecht, 300 p.

Clocchiatti, R., Condomines, M., Guénot, N., and Tanguy, J.C., 2004, Magma changes at Mount Etna: the 2001 and 2002–2003 eruptions. Earth and Planetary Science Letters, 226, 397–414. https://doi.org/10.1016/j.epsl.2004.07.039

Coltelli, M., Proietti, C., Branca, S., Marsella, M., Andronico, D., and Lodato, L., 2007, Analysis of the 2001 lava flow eruption of Mt. Etna from three-dimensional mapping. Journal of Geophysical Research, 112, F02029. https://doi.org/10.1029/2006JF000598

Cordonnier, B., Lev, E., and Garel, F., 2015, Benchmarking lava-flow models. In: Harris, A.J.L., De Groeve, T., Garel, F., and Carn, S.A. (eds.), Detecting, Modelling and Responding to Effusive Eruptions. Geological Society, London, Special Publications, 426. https://doi.org/http://doi.org/10.1144/SP426.7

Corsaro, R.A., 2005, Dynamics of 2004–2005 Mt. Etna effusive eruption as inferred from petrologic monitoring. Geophysical Research Letters, 32, L13302. https://doi.org/10.1029/2005GL022347

Corsaro, R.A., Andronico, D., Behncke, B., Branca, S., Caltabiano, T., Ciancitto, F., Cristaldi, A., De Beni, E., La Spina, A., Lodato, L., Miraglia, L., Neri, M., Salerno, G., Scollo, S., and Spata, G., 2017, Monitoring the December 2015 summit eruptions of Mt. Etna (Italy): implications on eruptive dynamics. Journal of Volcanology and Geothermal Research, 341, 53–69. https://doi.org/10.1016/j.jvolgeores.2017.04.018

Crosetto, M., Monserrat, O., Cuevas-González, M., Devanthéry, N., and Crippa, B., 2016, Persistent Scatterer Interferometry: a review. ISPRS Journal of Photogrammetry and Remote Sensing, 115, 78–89. https://doi.org/10.1016/j.isprsjprs.2015.10.011

De Beni, E., Cantarero, M., Neri, M., and Messina, A., 2021, Lava flows of Mt Etna, Italy: the 2019 eruption within the context of the last two decades (1999–2019). Journal of Maps, 17, 65–76. https://doi.org/10.1080/17445647.2020.1854131

De Novellis, V., Atzori, S., De Luca, C., Manzo, M., Valerio, E., Bonano, M., Cardaci, C., Castaldo, R., Di Bucci, D., Manunta, M., Onorato, G., Pepe, S., Solaro, G., Tizzani, P., Zinno, I., Neri, M., Lanari, R., and Casu, F., 2019, DInSAR analysis and analytical modeling of Mount Etna displacements: the December 2018 volcano-tectonic crisis. Geophysical Research Letters, 46, 5817–5827. https://doi.org/10.1029/2019GL082467

Dragoni, M., 1989, A dynamical model of lava flows cooling by radiation. Bulletin of Volcanology, 51, 88–95. https://doi.org/10.1007/BF01081978

Fadhillah, M.F., Hakim, W.L., Park, S., Kim, D., Park, Y., Kim, C., and Lee, C., 2022, Surface deformation simulation for InSAR detection using a machine learning approach on the hantangang river volca-

nic field?: a case study on the Orisan mountain. Frontiers in Environmental Science. https://doi.org/10.3389/fenvs.2022.968120

Ferretti, A., Prati, C., and Rocca, F., 2001, Permanent scatterers in SAR interferometry. IEEE Transactions on Geoscience and Remote Sensing, 39, 8–20. https://doi.org/10.1109/36.898661

Gheorghe, M. and Armaş, I., 2016, Comparison of Multi-temporal differential interferometry techniques applied to the measurement of Bucharest City subsidence. Procedia Environmental Sciences, 32, 221–229. https://doi.org/10.1016/j.proenv.2016.03.027

Giacomoni, P.P., Coltorti, M., Mollo, S., Ferlito, C., Braiato, M., and Scarlato, P., 2018, The 2011–2012 paroxysmal eruptions at Mt. Etna volcano: insights on the vertically zoned plumbing system. Journal of Volcanology and Geothermal Research, 349, 370–391. https://doi.org/10.1016/j.jvolgeores.2017.11.023

Hakim, W.L., Ramayanti, S., Park, S., Ko, B., Cheong, D.K., and Lee, C.W., 2022, Estimating the pre-historical volcanic eruption in the Hatangang River Volcanic Field: experimental and simulation study. Remote Sensing, 14. https://doi.org/10.3390/rs14040894

Harris, A.J.L. and Rowland, S.K., 2001, FLOWGO: a kinematic thermo-rheological model for lava flowing in a channel. Bulletin of Volcanology, 63, 20–44. https://doi.org/10.1007/s004450000120

Harris, A.J.L. and Rowland, S.K., 2015, Flowgo 2012. In: Carey, R., Cayol, V., Poland, M., and Weis, D. (eds.), Hawaiian Volcanoes: From Source to Surface. Geophysical Monograph Series, John Wiley & Sons, p. 457–481. https://doi.org/10.1002/9781118872079.ch21

Hong, S.H. and Wdowinski, S., 2011, Interferometric coherence analysis with high resolution space-borne synthetic aperture radar. 2011 3rd International Asia-Pacific Conference on Synthetic Aperture Radar, APSAR 2011, Seoul, Sep. 26–30, p. 485–486.

Hooper, A., 2008, A multi-temporal InSAR method incorporating both persistent scatterer and small baseline approaches. Geophysical Research Letters, 35, L16302. https://doi.org/10.1029/2008GL034654

Hooper, A., Bekaert, D., Spaans, K., and Arıkan, M., 2012, Recent advances in SAR interferometry time series analysis for measuring crustal deformation. Tectonophysics, 514–517, 1–13. https://doi.org/10.1016/J.TECTO.2011.10.013

Hooper, A. and Zebker, H.A., 2007, Phase unwrapping in three dimensions with application to InSAR time series. Journal of the Optical Society of America A, 24, 2737–2747. https://doi.org/10.1364/josaa.24.002737

Hooper, A., Zebker, H., Segall, P., and Kampes, B., 2004, A new method for measuring deformation on volcanoes and other natural terrains using InSAR persistent scatterers. Geophysical Research Letters, 31, L23611. https://doi.org/10.1029/2004GL021737

Lanari, R., Lundgren, P., and Sansosti, E., 1998, Dynamic deformation of Etna Volcano observed by satellite radar interferometry. Geophysical Research Letters, 25, 1541–1544. https://doi.org/10.1029/98GL00642

Lee, C.W., 2014, Baekdusan Volcano time-series analysis from 1992 to 1998 using multi-interferogram InSAR processing. Terrestrial, Atmospheric and Oceanic Sciences, 25, 743–754. https://doi.org/10.3319/TAO.2014.06.06.01(T)

Lee, C.W., Lu, Z., Jung, H.S., Won, J.S., and Dzurisin, D., 2010, Surface deformation of Augustine Volcano, 1992–2005, from multiple-interferogram processing using a refined small baseline subset (SBAS) inter-

ferometric synthetic aperture radar (InSAR) approach. In: Power, J.A., Coombs, M.L., and Freymueller, J.T. (eds.), The 2006 Eruption of Augustine Volcano, Alaska. US Geological Survey Professional Paper, 1769, p. 453–465. https://doi.org/10.3133/pp176918

Lee, C.W., Lu, Z., Won, J.S., Jung, H.S., and Dzurisin, D., 2013, Dynamic deformation of Seguam Island, Alaska, 1992–2008, from multi-interferogram InSAR processing. Journal of Volcanology and Geothermal Research, 260, 43–51. https://doi.org/10.1016/j.jvolgeores.2013.05.009

Lu, Z. and Dzurisin, D., 2014, Tectonic setting of Aleutian volcanism. In: InSAR Imaging of Aleutian Volcanoes. Springer, Berlin, p. 49–69. https://doi.org/10.1007/978-3-642-00348-6_4

Marquardt, D.W., 1963, An algorithm for least-squares estimation of nonlinear parameters. Journal of the Society for Industrial and Applied Mathematics, 11, 431–441. https://doi.org/10.1137/0111030

Massonnet, D., Briole, P., and Arnaud, A., 1995, Deflation of Mount Etna monitored by spaceborne radar interferometry. Nature, 375, 567–570. https://doi.org/10.1038/375567a0

Mossoux, S., Saey, M., Bartolini, S., Poppe, S., Canters, F., and Kervyn, M., 2016, Q-LAVHA: a flexible GIS plugin to simulate lava flows. Computers and Geosciences, 97, 98–109. https://doi.org/10.1016/j.cageo.2016.09.003

Mulas, M., Cioni, R., Andronico, D., and Mundula, F., 2016, The explosive activity of the 1669 Monti Rossi eruption at Mt. Etna (Italy). Journal of Volcanology and Geothermal Research, 328, 115–133. https://doi.org/10.1016/J.JVOLGEORES.2016.10.012

Neri, M., Acocella, V., and Behncke, B., 2004, The role of the Pernicana Fault System in the spreading of Mt. Etna (Italy) during the 2002–2003 eruption. Bulletin of Volcanology, 66, 417–430. https://doi.org/10.1007/s00445-003-0322-x

Neri, M., Acocella, V., Behncke, B., Maiolino, V., Ursino, A., and Velardita, R., 2005, Contrasting triggering mechanisms of the 2001 and 2002–2003 eruptions of Mount Etna (Italy). Journal of Volcanology and Geothermal Research, 144, 235–255. https://doi.org/10.1016/j.jvolgeores.2004.11.025

Neri, M., Casu, F., Acocella, V., Solaro, G., Pepe, S., Berardino, P., Sansosti, E., Caltabiano, T., Lundgren, P., and Lanari, R., 2009, Deformation and eruptions at Mt. Etna (Italy): a lesson from 15 years of observations. Geophysical Research Letters, 36, L02309. https://doi.org/10.1029/2008GL036151

Neri, M., De Maio, M., Crepaldi, S., Suozzi, E., Lavy, M., Marchionatti, F., Calvari, S., and Buongiorno, M.F., 2017, Topographic maps of Mount Etna's summit craters, updated to December 2015. Journal of Maps, 13, 674–683. https://doi.org/10.1080/17445647.2017.1352041

Newhall, C., Self, S., and Robock, A., 2018, Anticipating future Volcanic Explosivity Index (VEI) 7 eruptions and their chilling impacts. Geosphere, 14, 572–603. https://doi.org/10.1130/GES01513.1

Norini, G., De Beni, E., Andronico, D., Polacci, M., Burton, M., and Zucca, F., 2009, The 16 November 2006 flank collapse of the southeast crater at Mount Etna, Italy: study of the deposit and hazard assessment. Journal of Geophysical Research, 114, B02204. https://doi.org/10.1029/2008JB005779

Okada, Y., 1985, Surface deformation due to shear and tensile faults in a half-space. Bulletin of the Seismological Society of America, 75, 1135–1154. https://doi.org/10.1785/BSSA0750041135

Osmanoğlu, B., Sunar, F., Wdowinski, S., and Cabral-Cano, E., 2016, Time series analysis of InSAR data: methods and trends. ISPRS Journal of Photogrammetry and Remote Sensing, 115, 90–102. https://doi.org/10.1016/j.isprsjprs.2015.10.003

Pepe, A. and Calò, F., 2017, A review of interferometric synthetic aperture RADAR (InSAR) multi-track approaches for the retrieval of Earth's Surface displacements. Applied Sciences, 7, 1264. https://doi.org/10.3390/app7121264

Rodriguez-Gonzalez, A., Aulinas, M., Mossoux, S., Perez-Torrado, F.J., Fernandez-Turiel, J.L., Cabrera, M., and Prieto-Torrell, C., 2021, Comparison of real and simulated lava flows in the Holocene volcanism of Gran Canaria (Canary Islands, Spain) with Q-LavHA: contribution to volcanic hazard management. Natural Hazards, 107, 1785–1819. https://doi.org/10.1007/s11069-021-04660-6

Scollo, S., Boselli, A., Coltelli, M., Leto, G., Pisani, G., Prestifilippo, M., Spinelli, N., and Wang, X., 2015, Volcanic ash concentration during the 12 August 2011 Etna eruption. Geophysical Research Letters, 42, 2634–2641. https://doi.org/10.1002/2015GL063027

Sousa, J.J., Hooper, A.J., Hanssen, R.F., Bastos, L.C., and Ruiz, A.M., 2011, Persistent Scatterer InSAR: a comparison of methodologies based on a model of temporal deformation vs. spatial correlation selection criteria. Remote Sensing of Environment, 115, 2652–2663. https://doi.org/10.1016/j.rse.2011.05.021

Spampinato, S., Langer, H., Messina, A., and Falsaperla, S., 2019, Short-term detection of volcanic unrest at Mt. Etna by means of a multi-station warning system. Scientific Reports, 9, 6506. https://doi.org/10.1038/s41598-019-42930-3

Tarquini, S., Isola, I., Favalli, F., Mazzarini, M. Bisson, M.T. Pareschi, and Boschi., E., 2007, TINITALY/01: a new Triangular Irregular Network of Italy. Annals of Geophysics, 50, 407–425. https://doi.org/10.4401/ag-4424

Wright, T.J., Lu, Z., and Wicks, C., 2003, Source model for the Mw 6.7, 23 October 2002, Nenana Mountain Earthquake (Alaska) from InSAR. Geophysical Research Letters, 30, 30–33. https://doi.org/10.1029/2003GL018014

Wright, T.J., Parsons, B.E., Jackson, J.A., Haynes, M., Fielding, E.J., England, P.C., and Clarke, P.J., 1999, Source parameters of the 1 October 1995 Dinar (Turkey) earthquake from SAR interferometry and seismic bodywave modelling. Earth and Planetary Science Letters, 172, 23–37. https://doi.org/10.1016/S0012-821X(99)00186-7

Zebker, H.A. and Goldstein, R.M., 1985, Topographic Mapping from interferometric synthetic aperture radar observations. Journal of Geophysical Research, 91, 4993–4999. https://doi.org/10.1029/jb091ib05p04993